research papers

Crystal structure and doping in synthetic enstatite: an analysis of Li/Fe^{3+}-doped single-crystal samples

Paolo Ballirano,[a]* Beatrice Celata,[b] Alessandro Pacella,[a] Andrea Bloise[c] and Ferdinando Bosi[a]

[a]Department of Earth Sciences, Sapienza University of Rome, Piazzale Aldo Moro 5, I-00185, Rome, Italy, [b]Department of Energy Technologies and Renewable Sources, ENEA CR Casaccia, S. Maria di Galeria, 00123, Rome, Italy, and [c]Department of Biology, Ecology and Earth Science, University of Calabria, Via P. Bucci cubo 15b, I-87036, Arcavacata di Rende (CS), Italy. *Correspondence e-mail: paolo.ballirano@uniroma1.it

A series of Li$^+$/Fe^{3+}-doped enstatite crystals of composition Mg$_{(2–2x)}$Li$_x$Fe$_x$Si$_2$O$_6$ were synthesized and structurally characterized. Under the selected experimental conditions, we grew three crystals of *Pbca* orthopyroxene (OPX: x = 0.270–0.313) and two crystals of *Pbcn* protopyroxene (PPX: x = 0.156–0.164) using the flux-growth technique. The observed variation in the polyhedral volume and distortion of the *M*2 octahedron as a function of Li/Fe^{3+} doping suggests the presence of an upper limit, at least for the OPX samples. The same linear relation was observed between the polyhedral volume and ⟨*M*1—O⟩ bond length across all analysed samples, including the endmembers protoenstatite (PEN), orthoenstatite (OEN) and LiFe^{3+}Si$_2$O$_6$. It seems that the *M*2 octahedron plays a crucial role in stabilizing the pyroxene topology in either the PEN or the OEN form, because the PPX and OPX samples show two distinct linear relations between the *M*2O$_6$ polyhedral volume and ⟨*M*2—O⟩, with the PPX trend converging toward the parameters of the LiFe^{3+}Si$_2$O$_6$ endmember, whereas the OPX trend, including OEN, diverges largely from these parameters.

1. Introduction

Magnesium silicate Mg$_2$Si$_2$O$_6$ can occur in six polymorphic modifications. Two of them are orthorhombic, namely, *Pbcn* protoenstatite (PEN: Kanzaki & Xue, 2017) and *Pbca* orthoenstatite (OEN: Ganguly & Ghose, 1979; Sasaki *et al.*, 1982), whereas four monoclinic modifications have been described so far, namely, *P*2$_1$/*c* low-pressure/low-temperature clinoenstatite (LPCEN/LTCEN: Ohashi & Finger, 1976; Ohashi, 1984; Pannhorst, 1984), *C*2/*c* (metastable) high-temperature clinoenstatite (HTCEN: Yoshiasa *et al.*, 2013), *C*2/*c* high-pressure clinoenstatite (HPCEN: Angel *et al.*, 1992) and *P*2$_1$/*c* high-pressure clinoenstatite (HPCEN2: Lazarz *et al.*, 2019). PEN has not been found in nature and is stable in a relatively small low-pressure range (<1 GPa) at temperatures (T) exceeding 1000 °C, potentially up to its incongruent melting point at 1550 °C (Boyd *et al.*, 1964). OEN has a large stability field at low pressure extending from ∼600 °C (forsterite Mg$_2$SiO$_4$ + liquid) up to melting (except for the small field occupied by PEN) and is the polymorphic form ubiquitously found in both igneous and metamorphic rocks. LPCEN/LTCEN is uncommon in nature, and it has been synthesized at T < 566 °C, clearly indicating that it is the low-temperature form of Mg$_2$Si$_2$O$_6$. A simplified P–T diagram of Mg$_2$Si$_2$O$_6$ is shown in Fig. 1. Lithium-bearing olivines (Ballirano *et al.*, 2024) were initially chosen as a test case for modelling Li$^+$ + Fe^{3+} ↔ 2 Mg^{2+} coupled substitution in silicates. Next, we selected Mg$_2$Si$_2$O$_6$ for further investigation on
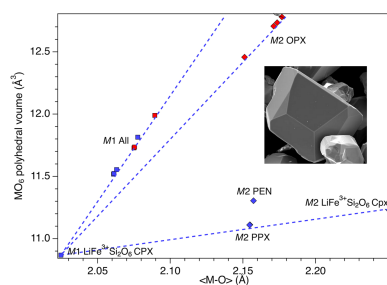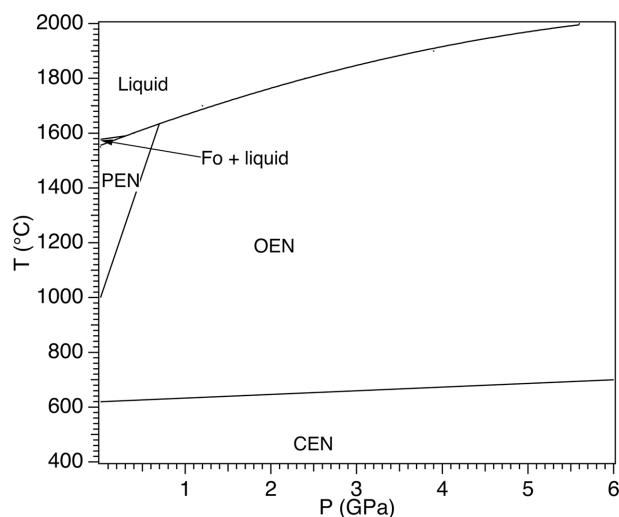
Figure 1
Simplified P–T diagram of $Mg_2Si_2O_6$. Abbreviations: protoenstatite (PEN), orthoenstatite (OEN), forsterite (Fo) and clinoenstatite (CEN).

this issue, owing to its capability to crystallize in different space groups. We focused, in particular, on the orthorhombic polymorphs of $Mg_2Si_2O_6$ as two synthetic *Pbcn* protopyroxene crystals of $Mg_{(2-2x)}Li_xSc_xSi_2O_6$ composition ($x = 0.23$ and 0.30) have been prepared and described so far (Smyth & Ito, 1977; Yang *et al.*, 1999), possibly suggesting that the partial coupled substitution (Li + $^{VI}Me^{3+}$) for 2Mg plays the role of stabilizer of such a pyroxene topology. Despite the small differences in the corresponding ionic radii (Li^+ = 0.760 Å and Sc^{3+} = 0.745 Å; Shannon, 1976), Li was fully ordered at the $M2$ site, whereas Sc^{3+} occupies the $M1$ site (Smyth & Ito, 1977; Yang *et al.*, 1999). However, upon recent revision of the ^{VI}Li ion radius to 0.812 Å (Hawthorne & Gagné, 2024), this site preference is perfectly explainable. The latter forms a polyhedron that is smaller and much less distorted compared to $M2O_6$. Owing to the significantly smaller ionic radius of Fe^{3+} compared to Sc^{3+} (0.649 *versus* 0.732 Å, respectively: Hawthorne & Gagné, 2024), we can hypothesize the onset of a similar ordering scheme for the $Li^+ + Fe^{3+} \leftrightarrow 2Mg^{2+}$ substitution. It is worth noting that the $LiFe^{3+}Si_2O_6$ endmember composition crystallizes as $C2/c$ clinopyroxene (Redhammer & Roth, 2004), with Li allotted at $M2$ and Fe^{3+} at $M1$. In the following, coordination polyhedra are denoted by the central cation site: thus, $M2$ octahedron.

According to the well-known MgO–SiO_2 phase diagram at room pressure, the synthesis of orthorhombic enstatite requires rather high temperatures. To decrease these temperatures, many studies have been carried out testing different synthesis procedures, such as the sol–gel technique (Mitchell *et al.*, 1998; Ban *et al.*, 1999; Douy, 2002) or the flux method (Ito, 1975; Grandin de L'éprevier & Ito, 1983; Ushio *et al.*, 1991) to obtain enstatite and forsterite. Although the sol–gel technique opens the way to the synthesis of impurity-free films, to obtain these in a crystalline form it is still necessary to use thermal treatment. Otherwise, the flux method is preferable for obtaining larger crystals and enhance doping (Smyth & Ito,

1977). During cooling, nutrient depletion in the melt and decreased solubility can alter the original molar ratios and lead to the formation of unintended mineral phases (Bloise *et al.*, 2009; Bloise *et al.*, 2011). As reported previously, $Mg_2Si_2O_6$ may crystallize as three polymorphs, leading to further complications: PEN, stable at high temperatures (1000–1575 °C), and OEN and LTCEN stable at lower temperatures, the extent of crystallization of which has been reported as depending on the cooling rate (Smyth, 1974; Ito, 1975; Catalano *et al.*, 2014). Consequently, slight variations in the synthesis conditions or the molar ratios can lead to the formation of additional phases, making it challenging to achieve stoichiometric control of the single phase due to the particular thermodynamic and kinetic conditions required.

For this work, crystals were grown using the flux-growth technique with lithium–vanadomolybdate as the melting agent (Ozima, 1982; Ozima & Akimoto, 1983; Grandin de L'éprevier & Ito, 1983). The acidity of the flux is crucial for enhancing the solubility of SiO_2 by converting it into orthosilicic acid $Si(OH)_4$. This can be done using MoO_3 and V_2O_5 together. Fluxes lacking either vanadate or molybdate are ineffective in solubilizing SiO_2 (Smyth & Ito, 1977; Ushio *et al.*, 1991). Indeed, MgO and SiO_2 exhibit minimal mutual reactivity, while the presence of silicic acid promotes the formation of Si—O—Mg bonds, hence favouring the formation of phases such as enstatite and forsterite (Douy, 2002; Gu *et al.*, 2018; Bloise *et al.*, 2009). The formation of $LiFeSi_2O_6$, which begins at 500 °C when CO_2 is released from the dissolution of Li_2CO_3 (Tanaka & Takei, 1997), plays a crucial role in lowering the formation temperature of pyroxenes and is responsible for their doping. This effect, as reported previously (*e.g.* Ito, 1975; Grandin de L'éprevier & Ito, 1983; Smyth & Ito, 1977), stabilizes PEN (the high-temperature polymorph of enstatite), thereby extending its stability range to lower temperatures.

The present work investigates the crystal chemistry of the $Li^+ + Fe^{3+} \leftrightarrow 2Mg^{2+}$ coupled substitution along the $Mg_2Si_2O_6$–$LiFe^{3+}Si_2O_6$ compositional joint by single-crystal X-ray diffraction (SCXRD). The incorporation of Li and Fe^{3+} can significantly influence the properties and behaviour of enstatite crystals, with possible implications as cathode materials for lithium-ion batteries (LiBs), given the interest generated by the first report on the electrochemical and structural properties of the pyroxene-type $LiFeSi_2O_6$ by Zhou *et al.* (2014).

2. Experimental

2.1. Synthesis

The route commonly used to synthesize Fe-doped enstatite crystals, ideally $Fe_{0.2}Mg_{1.8}Si_2O_6$, was followed. Granular quartz (SiO_2; code No. 364011), magnesium oxide (MgO; code No. 459586), metallic iron (Fe; code No. 451377) and hematite (Fe_2O_3; code No. 451824) from Carlo Erba (reagent grade with purity $\geq$ 98%) were used as the starting materials without further purification.

Pre-heating was necessary to enhance the reactivity between the starting materials: granular quartz was converted into cristobalite by heating the powdered SiO_2 to 1400 °C for 12 h, while MgO, Fe and Fe_2O_3 powders were heated for a week at 110 °C, to ensure complete dehydration. Iron(II) oxide was prepared through partial reduction of hematite by metallic iron, following the reaction: $1/3Fe + 1/3Fe_2O_3 = FeO$. Molybdenum(VI) oxide (MoO_3; code No. 267856), vanadium(V) oxide (V_2O_5; code No. 223794) and lithium carbonate (Li_2CO_3; code No. 62470) from Sigma–Aldrich (reagent grade with purity $\geq 98\%$) were used as flux. The flux composition was as follows: $MoO_3 = 55.9$ wt%, $V_2O_5 = 9.8$ wt% and $Li_2CO_3 = 34.3$ wt% (Bloise *et al.*, 2011). Approximately 1.25 g of finely powdered starting materials (grain size < 0.177 mm), prepared according to the ideal $Fe_{0.2}Mg_{1.8}Si_2O_6$ stoichiometry of Fe-doped enstatite, along with flux, were loaded into a 100 ml platinum crucible and placed in a vertical furnace. The lithium–vanadomolybdate flux was added to the starting materials/flux, maintaining a consistent starting materials (g)/ flux (g) ratio of 0.5.

Iron-doped enstatite crystals were grown in a furnace equipped with a Super Kanthal heating element (0–1700 °C), with temperature control provided by PtRh–PtRh thermocouples, with a precision of ±4 °C.

The thermal run proceeded as follows: a steep increment up to 1050 °C was followed by 100 h where the temperature was kept constant to bring about complete dissolution and homogenization of the mixture. The resulting melt was then cooled slowly to 650 °C at a rate of 1.25 °C h^{-1}, followed by rapid quenching to room temperature by immersion of the crucible in water.

The growth conditions for enstatite followed well-established protocols from the literature (Bloise *et al.*, 2011; Catalano *et al.*, 2014; Catalano *et al.*, 2015). As a result, orthopyroxene crystals with the composition $Mg_{(2-2x)}Li_x$-$Fe^{3+}_xSi_2O_6$ (0.15 < x < 0.31) were obtained. Euhedral colourless crystals, averaging 800 μm in length, were separated from the solidified flux by sonication in hot water. The crystals were recovered using a binocular microscope, selected and subsequently characterized by SCXRD.

2.2. Single-crystal X-ray diffraction

Five crystal fragments (labelled as **1**, **2**, **3**, **4a** and **4d**) were selected for X-ray diffraction measurements on a Bruker Kappa APEXII single-crystal diffractometer (Sapienza University of Rome, Earth Sciences Department), equipped with a CCD area detector (6.2 × 6.2 cm active detection area, 512 × 512 pixels) and a graphite-crystal monochromator, using Mo $K\alpha$ radiation from a fine-focus sealed X-ray tube. The sample-to-detector distance was 4 cm. Preliminary scrutiny of the reciprocal lattice of the samples clearly indicated their orthorhombic symmetry. Samples **1**, **2** and **3** have *Pbca* symmetry ($a \sim 18.17$ Å, $b \sim 8.77$ Å and $c \sim 5.19$ Å, *i.e.* that of orthopyroxenes OPX) and samples **4a** and **4d** have *Pbcn* symmetry (*i.e.* that of protopyroxenes PPX), showing a halved *a* parameter. Diffraction data for **1**, **2**, **4a** and **4d** were collected

up to $\sin \theta_{max}/\lambda = 1.000$ Å^{-1} and those for **3** up to $\sin \theta_{max}/\lambda = 1.184$ Å^{-1}.

A total of 1708 (and 1365 for sample **3**) exposures (step = 0.4°, time/step = 15 s) covering a full reciprocal sphere with a completeness > 96% and redundancy of approximately 5 were collected. Final unit-cell parameters were refined using the *SAINT* program (Bruker, 2016) with numbers of reflections ranging between 3347 and 9984, with $I > 10\sigma(I)$ in the range $6 < 2\theta < 91°$. The associated intensities of all collected reflections were processed and corrected for Lorentz and background effects plus polarization, using *APEX2* software (Bruker, 2016). The data were corrected for absorption using a multi-scan method (*SADABS*; Bruker, 2016). The absorption correction led to a significant improvement in $wR2_{int}$ (from about 0.04 to about 0.02).

2.3. Structure refinement

Structure refinements were carried out using *SHELXL2013* (Sheldrick, 2015) and *ShelXle* (Hübschle *et al.*, 2011). The starting coordinates were taken from Ganguly & Ghose (1979) for OPX (samples **1**, **2** and **3**) and from Smyth & Ito (1977) for PPX (samples **4a** and **4d**).

The key difference between the two orthorhombic pyroxene structures lies in their crystallographically distinct *T* and *O* sites. In *Pbcn* PPX, there is only one *T* site and three distinct *O* sites (O1, O2 and O3). In contrast, *Pbca* OPX has two distinct *T* sites (*T*1 and *T*2) and six distinct *O* sites (O1*a*, O1*b*, O2*a*, O2*b*, O3*a* and O3*b*). Both structures contain octahedrally coordinated cations at two distinct *M*1 and *M*2 sites.

The following parameters were refined: scale factor, extinction coefficient, atom coordinates, site-scattering values and anisotropic atomic displacement factors. In the starting stages of the refinements, Mg was used as the scatterer at the *M*1 and *M*2 sites. The observed excess of electron density at *M*1 and the deficiency in *M*2 indicated unequivocally the partition of Fe^{3+} at *M*1 and Li at *M*2. This scheme is analogous to that observed in Li/Sc PPX (Sc at *M*1 and Li at *M*2; Smyth & Ito, 1977). Subsequently, the *M*1 and *M*2 sites were modelled using Mg *versus* Fe and Mg *versus* Li scattering factors, respectively. A first set of refinements was done using neutral scattering curves for all atoms. Finally, following Hawthorne *et al.* (1995) and the results of Ballirano *et al.* (2021) for amphiboles and Ballirano *et al.* (2024) for Li/Fe^{3+}-doped olivines, further refinements were done modelling the *T*1 and *T*2 sites using the Si^0 *versus* Si^{4+} scattering factors, whereas the anion sites were modelled with the O^0 *versus* O^{2-} scattering factors. The coefficients for analytical approximation to the scattering factors were from Table 6.1.1.4 of the *International Tables for Crystallography* (Volume C; Brown *et al.*, 2006), the only exception being those of O^{2-} which were taken from Hovestreydt (1983). A significant improvement of the statistical indicators was observed passing from neutral to partly ionized scattering curves.

In the final stages of the refinement, it was observed that the site occupancy factor (sof) of Fe at *M*1 and of Li at *M*2 were almost coincident (the sof of Li at *M*2 slightly exceeding that

of Fe at $M1$: Δ = 0.003–0.013) and therefore they were constrained to be equal. The small discrepancy has been attributed to the presence of minor V^{3+} (ionic radius = 0.641 Å; Hawthorne & Gagné, 2024) replacing Fe^{3+}, owing to its smaller scattering power (23 versus 26 e^-). This result is an indirect proof that all iron occurs as Fe^{3+}. The application of this constraint did not affect the various statistical indicators.

Table S1 reports space groups, unit-cell parameters, $2\theta_{max}$ and $\sin\theta_{max}/\lambda$ of the various data collections, and relevant statistical indicators of the refinements. Table S2 lists the $M1$ and $M2$ site populations, the ion charges for O and Si, and the equivalent displacement parameters. Relevant bond distances and several parameters describing the extent of polyhedral distortion are reported in Table S3, and the results of a bond valence analysis in Table S4.

Figure 3
Dependence of the b parameter from the Li sof. The red dashed curve is a guide to the eye showing the variation of Li in the PPX. The linear fit of the variation of Li in the OPX is reported as a blue solid line.

3. Results and discussion

Refinements substantially confirmed the findings of Ballirano et al. (2021, 2024) regarding the use of partially ionized scattering curves of O and Si for tremolite and olivine to empirically compensate for perturbation of the electron density caused by the interaction with other atoms (Table S2 in the supporting information). The refined ion charges for O and Si were in the range −1.492 to −1.381 and 0.377 to 0.720, respectively.

OPX samples were characterized by a coupled Li/Fe^{3+} substitution level in the 0.270 (1)–0.313 (1) sof range, whereas PPX samples were in the 0.156 (1)–0.164 (1) sof range. This finding suggests that, under the present experimental conditions, the PPX topology is favoured at smaller doping levels than in the case of Li/Sc^{3+}, where crystals were obtained in the 0.23–0.30 sof range (Smyth & Ito, 1977; Yang et al., 1999).
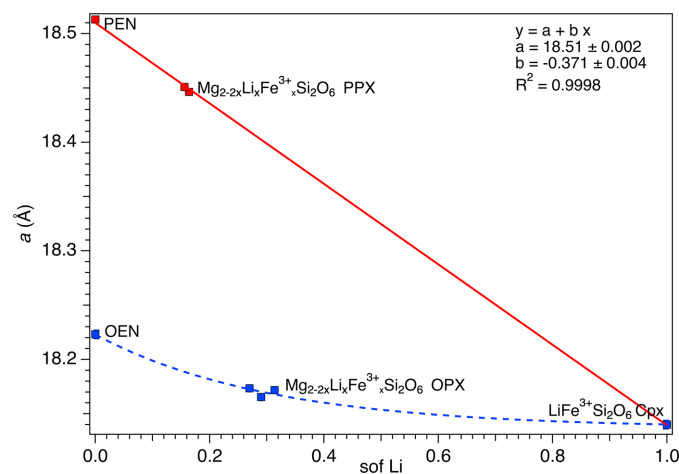
3.1. Unit-cell parameters

Unit-cell parameters as a function of composition are illustrated in Figs. 2–4 (see also Fig. S1 in the supporting information), where $LiFe^{3+}Si_2O_6$ was considered the common endmember for both the OPX and the PPX series. To obtain a comparable data set, the a parameter of $LiFe^{3+}Si_2O_6$ was recalculated based on an orthorhombic cell, according to the well-known relationship $a_{orth} = 2a_{mon}\sin\beta$, whereas for the PPX samples, the a parameter was multiplied by two, in both cases resulting in a doubled unit-cell volume. The OPX and PPX samples show a different behaviour for each unit-cell parameter, coherent with the significantly different volumes of the OEN and PEN endmembers. For OPX samples, the unit-cell volume dependence on composition follows a bell-shaped curve (i.e. intermediate compositions have a volume smaller than both endmembers), whereas there is a marked decrease

Figure 2
Dependence of the a parameter from the Li site occupancy factor (sof). The blue dashed curve is a guide to the eye showing the variation of Li in the OPX. The linear fit of the variation of Li in the PPX is reported as a red solid line. Cpx = clinopyroxene.
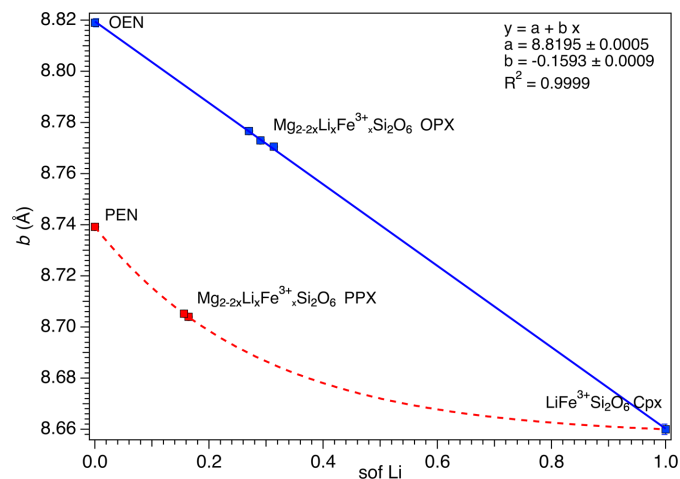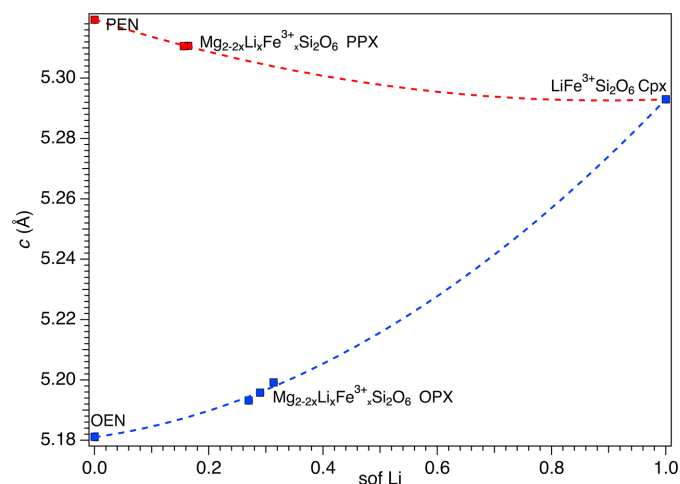

Figure 4
Dependence of the c parameter from the Li sof. The red and blue dashed curves are guides to the eye showing the variation of Li in the PPX and OPX, respectively.
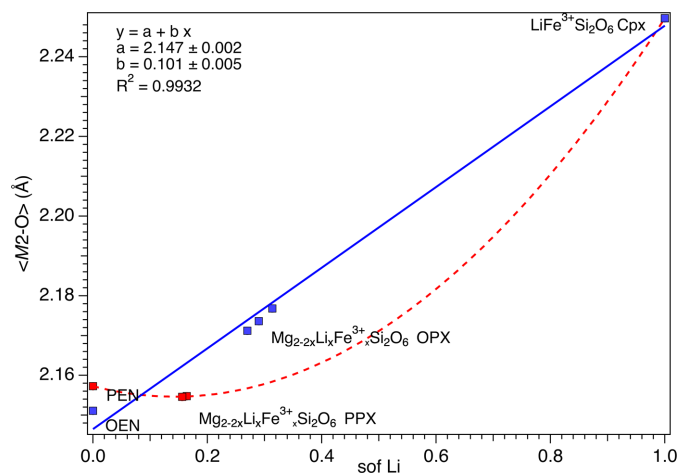
Figure 5
Variation of $\langle M2-O \rangle$ as a function of the Li sof. The red dashed curve is a guide to the eye showing the variation of Li in the PPX. The linear fit of the variation of Li in the OPX is reported as a blue solid line.

Figure 7
Variation of the volume of the $M2$ octahedron as a function of the Li sof.

from PEN to $LiFe^{3+}Si_2O_6$ (Fig. S1). For both series, the a unit-cell parameters contract from $Mg_2Si_2O_6$ to $LiFe^{3+}Si_2O_6$. However, the contraction is remarkably higher and linear for the PPX samples, whereas the trend is nonlinear and decreases at a significantly smaller rate for the OPX samples (Fig. 2). The trend in reversed in the case of the b unit-cell parameter (Fig. 3). Conversely, the c unit-cell parameter shows a strong expansion from OEN to $LiFe^{3+}Si_2O_6$, whereas the PPX series is characterized by a small contraction (Fig. 4). Both trends are nonlinear.

3.2. Structural features

Before discussing how the structural features of the two series of orthopyroxenes depend on their composition, it is worth noting that reference structural data for PEN were obtained through Rietveld refinement of laboratory powder
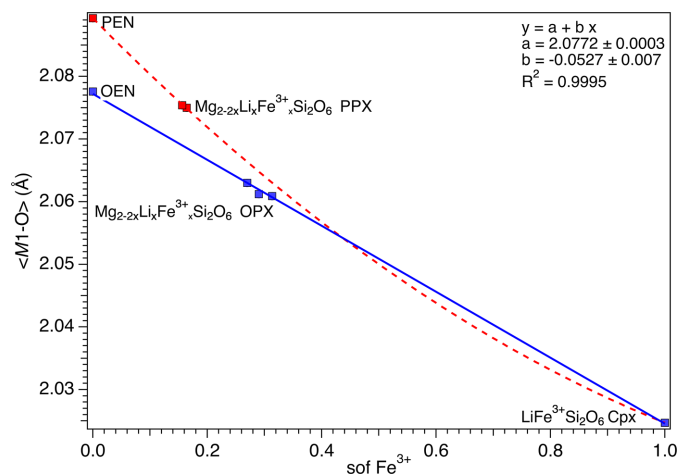
X-ray diffraction data collected in reflection mode (Kanzaki & Xue, 2017). However, no details of the refinement procedure were reported in the related article, particularly regarding the use of soft constraints on bond distances and how preferred orientation was accounted for. As a consequence, the accuracy of the structural parameters for PEN might be somewhat lower than that of the results. Therefore, any correlations drawn for PPX samples should be approached with some caution.

That said, unit-cell parameters and $\langle M1-O \rangle$ and $\langle M2-O \rangle$ show similar correlations with the Li/Fe^{3+} sof (Figs. 5 and 6). For the OPX samples, there is a noticeable increase of $\langle M2-O \rangle$ from OEM (2.151 Å) to $LiFe^{3+}Si_2O_6$ (2.249 Å). In contrast, in the case of the PPX samples, PEN has a slightly larger $\langle M2-O \rangle$ (2.157 Å) than OEN and the doped samples do not show appreciable variations from that value (2.155 Å), but they are still significantly lower than the $LiFe^{3+}Si_2O_6$ value. The $\langle M1-O \rangle$ decreases smoothly in both series of

Figure 6
Variation of $\langle M1-O \rangle$ as a function of the Fe^{3+} sof. The red dashed curve is a guide to the eye showing the variation of Fe^{3+} in the PPX. The linear fit of the variation of Fe^{3+} in the OPX is reported as a blue solid line.
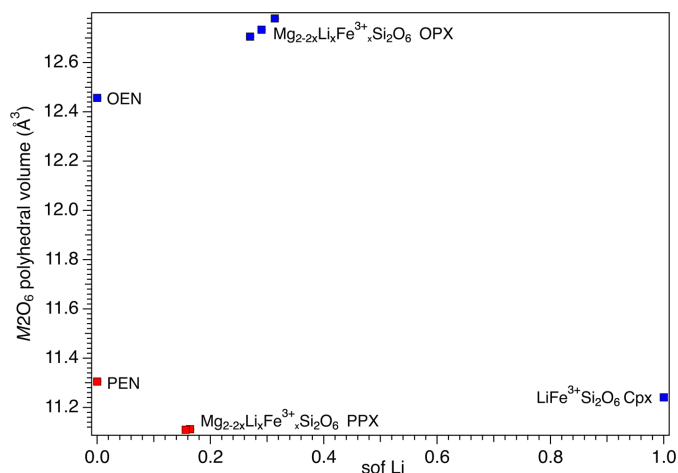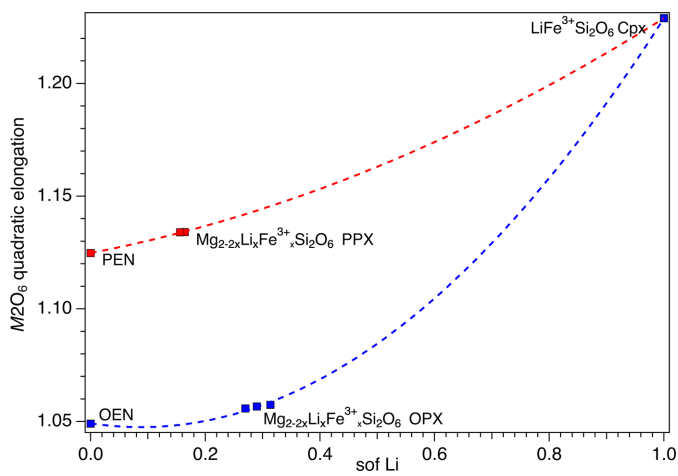

Figure 8
Variation of the quadratic elongation (QE) of the $M2$ octahedron as a function of the Li sof. The red and blue dashed curves are guides to the eye showing the variation of Li in the PPX and OPX, respectively.
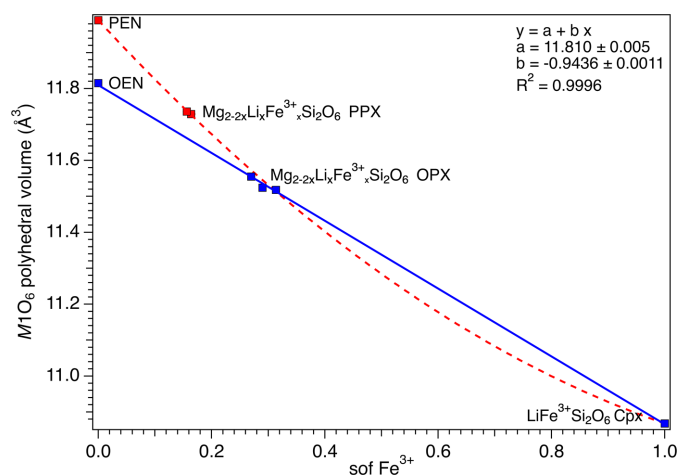
Figure 9
Variation of the volume of the $M1$ octahedron as a function of the Fe^{3+} sof. The red dashed curve is a guide to the eye showing the variation of Fe^{3+} in the PPX. The linear fit of the variation of Fe^{3+} in the OPX is reported as a blue solid line.

samples from 2.078 (OEN) or 2.089 (PEN) to 2.025 Å for $LiFe^{3+}Si_2O_6$. The trend for OPX is linear and almost linear for PPX if the value for PEN is accepted as accurate.

Analysis of the volume and deviation from ideal shape of the $M2$ and $M1$ octahedra (Figs. 7–11) took into consideration several parameters (Table S3): polyhedral volume (Swanson & Peterson, 1980), polyhedral volume distortion (Makovicky & Balić-Žunić, 1998), distortion index (Baur, 1974), mean quadratic elongation and bond angle variance (Robinson *et al.*, 1971), and effective coordination number (Hoppe, 1979). The volume of the $M2$ octahedron is larger than that of the $M1$ octahedron for the OPX series of samples ($\sim$12.7–12.8 Å^3 *versus* $\sim$11.5 Å^3; Figs. 7 and 9). Moreover, the $M2$ octahedron is significantly more distorted than the $M1$ octahedron, as indicated by the mean quadratic elongation of $\sim$1.06 *versus*
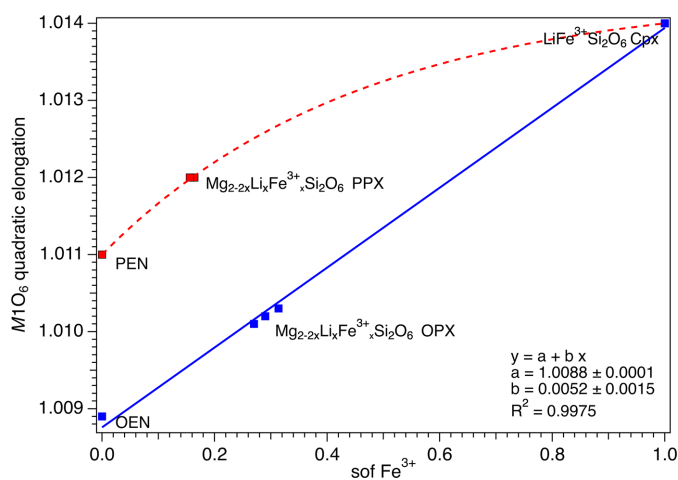

Figure 10
Variation of the quadratic elongation (QE) of the $M1$ octahedron as a function of the Li sof. The red dashed curve is a guide to the eye showing the variation of Fe^{3+} in the PPX. The linear fit of the variation of Fe^{3+} in the OPX is reported as a blue solid line.
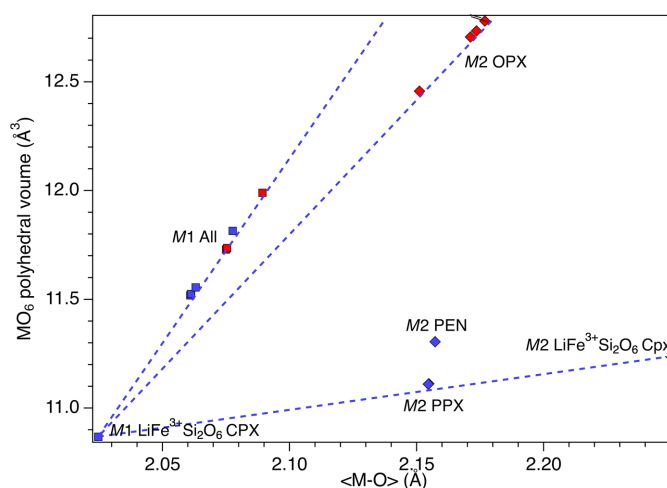

Figure 11
Variation of the polyhedral volume of the $M2$ and $M1$ octahedra as a function of $\langle M{-}O \rangle$. The dashed lines are guides to the eye. Key: red diamonds represent the $M2O_6$ polyhedral volume for OPX; blue diamonds the $M2O_6$ polyhedral volume for PPX, PEN and $LiFe^{3+}Si_2O_6$ Cpx; red squares the $M1O_6$ polyhedral volume for OPX; blue squares the $M1O_6$ polyhedral volume for PPX, PEN and $LiFe^{3+}Si_2O_6$. Cpx = clinopyroxene.

1.01. This same behaviour holds true for the $LiFe^{3+}Si_2O_6$ monoclinic endmember, in which the $M2$ octahedron has a very large quadratic elongation (1.229) typical of the Li-bearing clinopyroxenes (Cameron & Papike, 1981). In contrast, for the PPX samples, the polyhedral volume of the $M2$ octahedron is smaller than that of the $M1$ octahedron ($\sim$11.1 Å^3 *versus* $\sim$11.7 Å^3) and has a larger distortion, even larger than that of the OPX samples (mean quadratic elongation $\sim$1.13 *versus* 1.01). The smaller dimension of the $M2$ octahedron in the PEN and PPX samples with respect to the OPX samples is caused by the sharing of two edges of the octahedron with tetrahedra for the former, whereas in the case of the OEN and OPX samples, no polyhedral edges are shared (Cameron & Papike, 1981). Comparison of Figs. 7 and 8 suggests that for OEN and OPX samples, the increase of the volume of the $M2$ octahedron as a function of a growing level of doping is coupled to an increase in the mean quadratic elongation. In contrast, PEN and PPX samples do not show a well-defined dependence. OPX samples show an increase of the volume of the $M2$ octahedron with an increased level of doping and much larger than that of the $LiFe^{3+}Si_2O_6$ monoclinic endmember, whose volume is comparable to that of PPX but with a larger mean quadratic elongation value, much larger than for the OPX and PPX samples. This difference between OPX and $LiFe^{3+}Si_2O_6$ could potentially impose an upper limit on the level of coupled Li/Fe^{3+} substitution. Interestingly, recalculation of the original structural data of Smyth & Ito (1977) and Yang *et al.* (1999) for Li/Sc^{3+}-doped PPX samples (Table S3) results in mean quadratic elongations of the $M2$ octahedron (where a similar Li *versus* Mg substitution occurs) that aligns almost perfectly with the curve in Fig. 8 for the present Li/Fe^{3+}-doped PPX samples. In contrast, the polyhedral volume is slightly greater than that of PEN,

possibly suggesting that the value reported by Kanzaki & Xue (2017) is too large. Fig. 11 shows the variation in polyhedral volume of the $M2$ and $M1$ octahedra in Li/Fe^{3+}-doped orthopyroxenes as a function of $\langle M-O \rangle$. As can be seen, the volume of the $M1$ octahedron is linearly correlated with $\langle M-O \rangle$ for both OPX and PPX samples. Conversely, two separate dependences, one for OPX and one for PPX samples, are observed for the $M2$ octahedron. The displaced position of PEN from this trend suggests that the polyhedral volume of PEN is wrong (too large) and may possibly be related to a lower accuracy of the bond distances as arising from powder X-ray diffraction data with respect to the rest of the data set which is derived from single-crystal SREF.

Fig. S2 and Table S4 report the dependence of the bond valence sum at the various O sites. The parameters used for the calculations were taken from Gagné & Hawthorne (2015). Trends are clearly seen for the analysed samples and there are positive and negative deviations from the valence-sum rule.

4. Conclusions

In this study, we have investigated the crystal structure and doping of enstatite crystals with Li and Fe^{3+}. The incorporation of these dopants can significantly influence the properties and behaviour of enstatite crystals, making them interesting. Under the experimental conditions, we recovered five samples of $Mg_{(2-2x)}Li_xFe^{3+}_xSi_2O_6$ pyroxenes, namely, three orthopyroxene (OPX) with $0.270 < x < 0.313$ and two clinopyroxene (PPX) with $0.156 < x < 0.164$. This shows that varying levels of doping preferentially affect the pyroxene topologies.

Analysis of the ship between the volume and distortion of the $M2$ octahedron *versus* the level of doping indicates a possible upper limit for the coupled substitution of (Li + Fe^{3+}) for Mg, at least for OPX. The significant role of this polyhedron in stabilizing a specific pyroxene topology is further supported by the observation that for all analysed samples (including the endmembers PEN, OEN and LiFe^{3+}Si$_2$O$_6$), the relationship between the polyhedral volume and $\langle M1-O \rangle$ is linear. Conversely, there are two distinct linear relations for PPX and OPX samples between the $M2O_6$ polyhedral volume and $\langle M2-O \rangle$, with only the PPX trend converging toward the LiFe^{3+}Si$_2$O$_6$ endmember. Notably, the smaller $M2$ octahedron in PPX shares two edges with Si tetrahedra, whereas the larger $M2$ octahedron in OPX does not share two edges with Si tetrahedra.

This research enhances the understanding of crystal structure and doping in enstatite crystals, suggesting a potential use of Li/Fe^{3+}-doped enstatite in energy storage devices where a very stable structural framework is required for long-term Li$^+$ ion extraction/insertion.

5. Related literature

The following references are cited in the supporting information: Ilinca (2022); Momma & Izumi (2011).

References

Angel, R. J., Chopelas, A. & Ross, N. L. (1992). *Nature*, **358**, 322–324.
Ballirano, P., Celata, B., Pacella, A., Bloise, A., Tempesta, G., Sejkora, J. & Bosi, F. (2024). *Inorg. Chem.* **63**, 20372–20379.
Ballirano, P., Celata, B., Pacella, A. & Bosi, F. (2021). *Acta Cryst.* B**77**, 537–549.
Ban, T., Ohya, Y. & Takahashi, Y. (1999). *J. Am. Ceram. Soc.* **82**, 22–26.
Baur, W. H. (1974). *Acta Cryst.* B**30**, 1195–1215.
Bloise, A., Barrese, E., Apollaro, C. & Miriello, D. (2009). *Cryst. Res. Technol.* **44**, 463–468.
Bloise, A., Pingitore, V., Miriello, D., Apollaro, C., Armentano, D., Barrese, E. & Oliva, A. (2011). *J. Cryst. Growth*, **329**, 86–91.
Boyd, F. R., England, J. L. & Davis, B. T. C. (1964). *J. Geophys. Res.* **69**, 2101–2109.
Brown, P. J., Fox, A. G., Maslen, E. N., O'Keefe, M. A. & Willis, B. T. M. (2006). *International Tables for Crystallography*, Vol. C, edited by E. Prince, pp. 554–595. Dordrecht: Kluwer Academic Publishers.
Bruker (2016). *APEX, SAINT* and *SADABS*. Bruker AXS Inc., Madison, Wisconsin, USA.
Cameron, M. & Papike, J. J. (1981). *Am. Mineral.* **66**, 1–50.
Catalano, M., Bloise, A., Pingitore, V., Cazzanelli, E., Giarola, M., Mariotto, G. & Barrese, E. (2015). *Appl. Phys. A*, **120**, 175–182.
Catalano, M., Bloise, A., Pingitore, V., Miriello, D., Cazzanelli, E., Giarola, M., Mariotto, G. & Barrese, E. (2014). *Cryst. Res. Technol.* **49**, 736–742.
Douy, A. (2002). *J. Sol-Gel Sci. Technol.* **24**, 221–228.
Gagné, O. C. & Hawthorne, F. C. (2015). *Acta Cryst.* B**71**, 562–578.
Ganguly, J. & Ghose, S. (1979). *Contr. Miner. Petrol.* **69**, 375–385.
Grandin de L'éprevier, A. & Ito, J. (1983). *J. Cryst. Growth*, **64**, 411–412.
Gu, F., Peng, Z., Tang, H., Ye, L., Tian, W., Liang, G., Rao, M., Zhang, Y., Li, G. & Jiang, T. (2018). *Preparation of refractory materials from ferronickel slag*, in *Characterization of Minerals, Metals, and Materials 2018*, pp. 633–642. Cham, Switzerland: Springer.
Hawthorne, F. C. & Gagné, O. C. (2024). *Acta Cryst.* B**80**, 326–339.
Hawthorne, F. C., Ungaretti, L. & Oberti, R. (1995). *Can. Mineral.* **33**, 907–911.
Hoppe, R. (1979). *Z. Kristallogr.* **150**, 23–52.
Hovestreydt, E. (1983). *Acta Cryst.* A**39**, 268–269.
Hübschle, C. B., Sheldrick, G. M. & Dittrich, B. (2011). *J. Appl. Cryst.* **44**, 1281–1284.
Ilinca, G. (2022). *Minerals*, **12**, 924.
Ito, J. (1975). *Geophys. Res. Lett.* **2**, 533–536.
Kanzaki, M. & Xue, X. (2017). *J. Mineral. Petrol. Sci.* **112**, 359–364.
Lazarz, J. D., Dera, P., Hu, Y., Meng, Y., Bina, C. R. & Jacobsen, S. D. (2019). *Am. Mineral.* **104**, 897–904.
Makovicky, E. & Balić-Žunić, T. (1998). *Acta Cryst.* B**54**, 766–773.

Mitchell, M. B., Jackson, D. & James, P. F. (1998). *J. Sol-Gel Sci. Technol.* **13**, 359–364.

Momma, K. & Izumi, F. (2011). *J. Appl. Cryst.* **44**, 1272–1276.

Ohashi, Y. (1984). *Phys. Chem. Miner.* **10**, 217–229.

Ohashi, Y. & Finger, L. W. (1976). *Carnegie Inst. Washington Yearb.* **75**, 743–746.

Ozima, M. (1982). *J. Jpn Assoc. Mineral. Petrol. Econ. Geol.* **3**, 97–103.

Ozima, M. & Akimoto, S. (1983). *Am. Mineral.* **68** 1199–1205.

Pannhorst, W. (1984). *Neues Jb. Miner. Abh.* **150**, 219–228.

Redhammer, G. J. & Roth, G. (2004). *Z. Kristallogr.* **219**, 278–294.

Robinson, K., Gibbs, G. V. & Ribbe, P. H. (1971). *Science*, **172**, 567–570.

Sasaki, S., Fujino, K., Takeuchi, Y. & Sadanaga, R. (1982). *Z. Kristallogr.* **158**, 279–297.

Shannon, R. D. (1976). *Acta Cryst.* A**32**, 751–767.

Sheldrick, G. M. (2015). *Acta Cryst.* C**71**, 3–8.

Smyth, J. (1974). *Am. Mineral.* **59**, 345–352.

Smyth, J. R. & Ito, J. (1977). *Am. Mineral.* **62**, 1252–1257.

Swanson, D. K. & Peterson, R. C. (1980). *Can. Mineral.* **18**, 153–156.

Tanaka, T. & Takei, H. (1997). *J. Cryst. Growth*, **180**, 206–211.

Ushio, M., Kobayashi, N., Suzuki, M. & Sumiyoshi, Y. (1991). *J. Am. Ceram. Soc.* **74**, 1654–1657.

Yang, H., Finger, L. W., Conrad, P. G., Prewit, C. T. & Hazen, R. M. (1999). *Am. Mineral.* **84**, 245–256.

Yoshiasa, A., Nakatsuka, A., Okube, M. & Katsura, T. (2013). *Acta Cryst.* B**69**, 541–546.

Zhou, S., King, G., Scanlon, D. O., Sougrati, M. T. & Melot, B. C. (2014). *J. Electrochem. Soc.* **161**, A1642–A1647.